Computed Pore Potentials of the Nicotinic Acetylcholine Receptor

Robert H. Meltzer,* Wanda Vila-Carriles,* Jerry O. Ebalunode,† James M. Briggs,† and Steen E. Pedersen*
*Department of Molecular Physiology and Biophysics, Baylor College of Medicine, Houston, Texas 77035; and †Department of Biology and Biochemistry, University of Houston, Houston, Texas 77204

ABSTRACT Electrostatic surface potentials in the vestibule of the nicotinic acetylcholine receptor (nAChR) were computed from structural models using the University of Houston Brownian Dynamics program to determine their effect on ion conduction and ionic selectivity. To further determine whether computed potentials accurately reflect the electrostatic environment of the channel, the potentials were used to predict the rate constants for diffusion-enhanced fluorescence energy transfer; the calculated energy transfer rates are directly comparable with those determined experimentally (see companion article by Meltzer et al. in this issue). To include any effects on the local potentials by the bound acceptor fluorophore crystal violet, its binding site was first localized within the pore by fluorescence energy transfer measurements from dansyl-C6-choline bound to the agonist sites and also by simulations of binding using Autodock. To compare the computed potentials with those determined experimentally, we used the predicted energy transfer rates from Tb^{3+} chelates of varying charge to calculate an expected potential using the Boltzmann relationship. This expected potential (from −20 to −40 mV) overestimates the values determined experimentally (from −10 to −25 mV) by two- to fourfold at similar conditions of ionic strength. Although the results indicate a basic discrepancy between experimental and computed surface potentials, both methods demonstrate that the vestibular potential has a relatively small effect on conduction and selectivity.

INTRODUCTION

Ion conduction through the central pore of the nicotinic acetylcholine receptor (nAChR) is at least partly determined by the electrostatic environment within the solvent-accessible lumen of the protein: rings of negatively charged amino acids at the extracellular and intracellular mouths of the M2 α-helical transmembrane pore region, in particular, affect channel conductivity (1). Theoretical and computational treatment of low-resolution model systems of the transmembrane α-helices, arranged in a symmetrical pentameric bundle of the nAChR, has provided further insight into the role of the charges (2–5). These studies indicate that a substantial electronegative surface potential may be generated by the close proximity of conserved charges at the extracellular and intracellular mouths of the transmembrane spanning domain. Inclusion of negative charges distributed evenly about the surface of the extracellular vestibule enhances the electrostatic potential within the narrow ion channel to a level that may account for ionic selectivity (3). These approaches suggest that ionic selectivity and conduction are strongly influenced by local electrostatic surface potentials within the extracellular vestibule.

For ion channels in particular, the use of such a priori approaches is critical for understanding the structural basis of ionic selectivity and ionic conductivity. In general, however, computed electrostatic surface potentials are rarely compared explicitly with experimental data (for one exception, see 6) because most experimental methods for determining the effects of electrostatics do not provide an explicit value for the potential. Exceptions are methods that examine differences in local concentration that result from charge changes, such as the substituted-cysteine accessibility method (7). When applied to the nAChR in the open state, this approach revealed a strong intrinsic potential (from −230 to −100 mV) near the intracellular end of the M2 pore-lining α-helix that decreased toward the extracellular end of the pore to values ranging from −50 to +50 mV. Diffusion-enhanced fluorescence energy transfer (DEFET) also measures changes in local concentration near an acceptor chromophore and has the advantage that DEFET rates can be computed from the structural and electrostatic environment of the acceptor and the optical properties of the fluorophores (8,9). This provides a direct link between the DEFET measurement and the computed potential. In this work we examine this link using the measurements of the influence of electrostatic potentials on the distribution of variously charged Tb^{3+}-chelates about the binding site of the fluorescent noncompetitive antagonist crystal violet (CrV) within the channel of the nAChR (10). These experiments revealed the presence of a modest electronegative potential, −25 mV, that was attenuated by physiological ionic strength to −10 mV.

One goal of this work was to establish a direct relation between experimentally determined potentials and those determined by computational modeling to better evaluate the role of the outer ring of charges and the extracellular vestibule on ion conduction and ionic selectivity. A particular concern of continuum electrostatic calculations is that the surface topology may skew the calculations in highly

Submitted January 16, 2006, and accepted for publication May 17, 2006.

Address reprint requests to Steen E. Pedersen, Dept. of Molecular Physiology, Baylor College of Medicine, One Baylor Plaza, Houston, TX 77030. Tel.: 713-798-3888; E-mail: pedersen@bcm.tmc.edu.

The present address for Robert H. Meltzer and Wanda Vila-Carriles is Dept. of Physiology & Biophysics, University of Alabama, Birmingham, AL.

0006-3495/06/08/1325/11 $2.00

doi: 10.1529/biophysj.106.081455

constrained cases, such as the nAChR vestibule, where the effect of ionic strength may be overestimated (11) because the volume is too small to include a significant number of ions at any one time. To determine whether the surface potentials determined by DEFET, which are small in magnitude, are consistent with continuum electrostatics, we compared the basic DEFET parameters from a structural model of the nAChR. A homology model of the ion conductive pathway of the *Torpedo californica* muscle-type nAChR including both the ligand-binding domain and the transmembrane domain was used to compute electrostatic potentials. The computed electrostatic surface potential shows the presence of several strongly negative locations along the conductive pathway: one near the middle of the vestibule that appears to cause inward rectification and a second at the outer ring of charges near the extracellular end of the M2 α-helix. Comparison of actual DEFET-based potential estimates to simulated DEFET-based potentials, using the computed surface potential, reveals a consistent overestimate of experiment by the computed value. Possible sources for the discrepancy are discussed and suggest caution in interpretation of surface potentials without experimental correlation.

MATERIALS AND METHODS

Materials

CrV and phencyclidine were purchased from Aldrich Chemical (Milwaukee, WI), and CrV was prepared as described in our previous article (10). Dansyl-C6-choline (DC6C) was synthesized as described (12,13). nAChR-rich membranes were prepared from *Torpedo* electric organ as described previously (10).

FRET measurements

Fluorescence measurements were collected on an SLM (Champaign-Urbana, IL) 8000C fluorometer or on an ISS (Champaign-Urbana, IL) PC1 fluorometer. To limit the possible CrV binding sites within the nAChR, the distance between CrV and the bound fluorescent agonist DC6C was measured using FRET. The distance (R) between the donor and acceptor fluorophores is related to the efficiency of energy transfer (E).

$$R = R_0(1/E - 1)^{1/6} \tag{1}$$

$$R_0 = 9765(JQ_0\kappa^2\eta^{-4})^{1/6}\ \text{Å}. \tag{2}$$

R_0 is the distance at which energy transfer is 50% efficient. Q_0, the quantum yield of the donor, was 0.14 (14). κ^2 describes the relative orientation of the donor and acceptor fluorophores, and η is the refractive index of the environment (15). J is the overlap integral between the donor emission spectrum, $F(\lambda)$, and the acceptor absorbance spectrum $\varepsilon(\lambda)$.

$$J = \int_0^\infty F(\lambda)\varepsilon(\lambda)\lambda^4 d\lambda \Big/ \int_0^\infty F(\lambda)d\lambda\ \text{M}^{-1}\text{cm}^3. \tag{3}$$

Fluorescence emission spectra for 50 nM DC6C bound to 200 nM nAChR in HTPS (250 mM NaCl, 5 mM KCl, 3 mM $CaCl_2$, 2 mM $MgCl_2$, 20 mM HEPES, pH 7.0) were measured at room temperature through tryptophan energy transfer using excitation at 295 nm. Nonspecific fluorescence due to free DC6C and to intrinsic membrane fluorescence was subtracted; control samples were blocked at the agonist binding site with 1 mM carbamylcholine. Absorbance spectra for bound and free CrV to the nAChR were determined previously (16) and used after conversion of absorbance to extinction coefficients from the CrV concentration. Energy transfer was measured by donor quenching of bound DC6C emission in the presence of increasing concentrations of CrV. FRET efficiency, E, at each CrV concentration was calculated from the integrated DC6C emission spectra in the presence (F_{CrV}) and absence (F_0) of CrV ($E = (F_0 - F_{CrV})/F_0$). A plot of energy transfer efficiency versus CrV concentration can determine the FRET efficiency for stoichiometric occupation of the CrV sites (14,17) by extrapolation. The uncertainty in the dipole orientation factor κ^2 was examined using the fluorescence anisotropies (r_0) of the donor and acceptor fluorophores according to Dale et al. (18). Fluorescence anisotropy was measured for CrV and DC6C when bound to excess nAChR on the SLM 8000 fluorometer using film polarizers.

$$\kappa^2_{\text{max}} = 2/3 * (1 + \langle d^x_D\rangle + \langle d^x_A\rangle + 3\langle d^x_D\rangle\langle d^x_A\rangle \tag{4}$$

$$\kappa^2_{\text{min}} = 2/3 * [1 - (\langle d^x_D\rangle\langle d^x_A\rangle)/2], \tag{5}$$

where

$$\langle d^x\rangle^2 = r_0/0.4. \tag{6}$$

CrV fluorescence was determined with excitation at 550 and 590 nm. DC6C fluorescence was excited through direct fluorophore stimulation at 340 nm.

Structural modeling

To construct a model of the ligand-binding domain of the *Torpedo californica* nAChR, we aligned the N-terminal, extracellular α-, β-, δ-, γ-subunit sequences (accession No. PO2710, PO2712, PO2714, and PO2718 (19,20,21)) simultaneously with the sequence of the acetylcholine binding protein (AChBP, NCBI accession No. 1I9B) using parallel PRRN (22). The sequence alignment was further adjusted to maintain a register of structurally important residues as identified by sequence conservation, function, or surface exposure (23). The initial homology model was built by threading the aligned sequences individually into the structure of an AChBP subunit using SwissModel as accessed through DeepView/Swiss-PdbViewer 3.7 (24). The subunits were then assembled into a pentamer based on the coordinates of the AChBP subunits. Bad side-chain contacts at the interfaces of the subunits were resolved using DeepView (24) or adjusted manually, and energy minimized in Hyperchem (version 5.1, Hypercube, Gainesville, FL) using the BIO+ implementation of the CHARMM parameter set (25).

The structure of the *Torpedo* nAChR transmembrane domain (accession No. 1OED; (26)) was aligned coaxially with the extracellular homology model and positioned such that the C-terminal residues of the extracellular domain and the N-terminal residues of the transmembrane domain were closely apposed. The seven disulfide bonds present in the structure were defined explicitly, and the entire structure of the nAChR model was energy minimized in CHARMM developmental version 27b3 using 500 steps of steepest descent followed by 500 steps of conjugate-gradient minimization.

DC6C was modeled into the agonist binding sites by positioning its quaternary ammonium at the coordinates of the HEPES ethyl piperazine ammonium in the crystal structure of AChBP (27). DC6C was then energy minimized using Hyperchem with MM+ parameters using steepest descent and conjugate gradient algorithms. CrV was initially positioned along the central pore axis with the distance between the CrV central carbon and the DC6C chromophore constrained by the FRET measurement to 50 Å. CrV was then energy minimized. The partial charge distribution on CrV in the bound conformation was derived from semiempirical quantum mechanics using the AM1 Hamiltonian (28) in Hyperchem and appended to the University of Houston Brownian Dynamics (UHBD) parameter file. CrV binding was also modeled using Autodock 3.05 (29). Models for the ligand

and the energy-minimized structure of the nAChR were prepared using Autodock Tools. A 96 × 96 × 126 point grid with 0.25-Å spacing was prepared centered on the axis of the receptor. Then, 100 docking rounds were performed with 50 randomly distributed initial structures of CrV in each run. All runs were subjected to 15 million rounds of energy evaluation. The lowest-energy bound structure from each run was saved, and the lowest-energy structures were binned in clusters by RMSD less than 1.5 Å.

Electrostatic computations and simulation of DEFET

The pK_a values of all nAChR titratable residues were predicted with the UHBD program (30) using the methods of Bashford and Karplus (31). The energy-minimized homology structure of the AChR was prepared for UHBD by protonating the protein in a fully neutral state. All histidines were assumed to be monoprotonated, and disulfide-bonded cysteines were identified explicitly. pK_a assignments were predicted for the nAChR in 20, 150, and 300 mM ionic strength and for the structure with bound CrV. The predicted ionization states for titratable residues at various pH values were used to compute the electrostatic potential of the system. The electrostatic environment about the entire nAChR model was computed using the nonlinearized form of the Poisson-Boltzmann equation. The potential about the protein was solved on a 65 × 65 × 65 point grid. For DEFET integration, high-resolution potential maps in the region of the acceptor were generated using the results of lower-resolution maps as boundary conditions. The grid was aligned with the lumen of the nAChR, and axial potential profiles were extracted directly from the Poisson-Boltzmann computation results.

The bimolecular rate constants (k_2^x) of DEFET from Tb^{3+} chelates to CrV were computed by numerically integrating Eq. 7 over all accessible space (9). R_0 is the Förster distance of fluorescent energy transfer, τ_0 is the intrinsic luminescent lifetime of the donor fluorophore in the absence of acceptor, r_{et} is the distance between the donor and acceptor fluorophores, and the exponential term the dependence of the charged donor fluorophore concentration on the electrostatic field $w(r)$; k_B is Boltzmann's constant.

$$k_2 = 0.6023\frac{R_0^6}{\tau_0}\iiint r_{et}^{-6} e^{-k_B Tw(r)} dV \,\mathrm{M}^{-1}\mathrm{s}^{-1}. \quad (7)$$

Numerical integrations of k_2^x values were solved on a 65 × 65 × 65 point grid with 0.75-Å spacing by summing the contribution to k_2^x at each voxel. The integrated space was determined by including only the points accessible to a rolling sphere with a radius corresponding to the chelate radius. Because of the r^{-6} distance dependence, the volume outside this grid does not contribute substantially to the k_2^x values. The energy transfer distance at each voxel was based on the distance from the voxel either to the closest atom in the structure of CrV (method 1) or to the central carbon of CrV (method 2). The orientation factor κ^2 was solved explicitly for every point while assuming isotropic emission from Tb^{3+}-chelates and circularly symmetric absorption dipoles within the plane of bound CrV. The chelate radius should be in the range of 4–6 Å, but the exact choice strongly affects the k_2^x values. The results of the integration also depended on the choice of grid size and spacing and the method used to define the energy transfer distance, but these variables had less effect on the result than did the choice of chelate radius. Approximate electrostatic potentials were then back-calculated from the predicted rates of DEFET (10):

$$\psi = \frac{k_B T}{e}\ln\frac{k_2^+}{k_2^0} = \frac{k_B T}{e}\ln\frac{k_2^0}{k_2^-}, \quad (8)$$

where e is the unit electron charge, and k_2^x is the measured bimolecular rate of energy transfer for the positive, neutral, or negative chelates.

The relative flux of ions through the nAChR was calculated with an equation derived from the Poisson-Nernst-Plank equation (32).

$$J_{ion} = \frac{\exp\left(\frac{q_i F \Delta\phi_{TM}}{RT}\right) - 1}{\int \exp\left(\frac{q_i F(\phi_{Channel}(z) + \phi_{TM}(z))}{RT}\right) dz}. \quad (9)$$

Here, the flux of ions J_{ion} is dependent on both the potential profiles of the ion channel ($\phi_{Channel}$) as predicted from the Poisson-Boltzmann profiles and on the transmembrane potential (ϕ_{TM}). The transmembrane potential was modeled as a linear gradient across the membrane-spanning region of the protein, with 0 mV at the extracellular surface and −100–100 mV in 20-mV steps for the intracellular potential.

RESULTS

In the previous article (10) we utilized lanthanide-based DEFET measurements to determine the local electrostatic potential near a nAChR-bound noncompetitive antagonist, CrV. To interpret the effects of this potential on nAChR function and to directly compare computed and experimental potentials in the vestibule of the nAChR, we determined the binding locus of CrV by FRET measurements and by Autodock simulations of CrV-binding to a nAChR structural model.

Localization of the CrV binding site by FRET and by Autodock simulation

A threaded homology model of the nAChR extracellular domain was generated based on sequence alignment of the *Torpedo* AChR subunits with the AChBP. One or two amino acid insertions at several loops between β-sheet segments were resolved using SwissModel without perturbing the overall structure. A nAChR-nonconserved proline, αPro197, in the binding site loop C was removed from the nAChR sequence for threading to achieve proper indexing within the loop and was then reinserted into the threaded structure and energy minimized. This procedure retained the positions of critical binding-site residues; conserved residues at the nAChR agonist-binding sites in the homology model had an average RMSD of 1 Å compared with the AChBP structure; the average RMSD for all conserved residues was 2.6 Å. The nAChR β-, γ-, and δ-subunit sequences include 8–12 unaligned amino acids between AChBP residues 157 and 158. Because these regions had no structural basis for modeling, they returned from the algorithm as unstructured and were subsequently energy minimized with the rest of the protein.

The assembled, pentameric, extracellular domain was then apposed to the transmembrane domain, and the complete structure energy minimized with occasional adjustment of loops in both domains to achieve a good fit. The resultant structure has the last residue of the extracellular domain within bonding distance to the amino-terminus of the transmembrane domain (Fig. 1 *A*). The model was also consistent with the predictions of surface-exposed and buried residues for all subunits compiled from lysine scanning mutagenesis experiments (23).

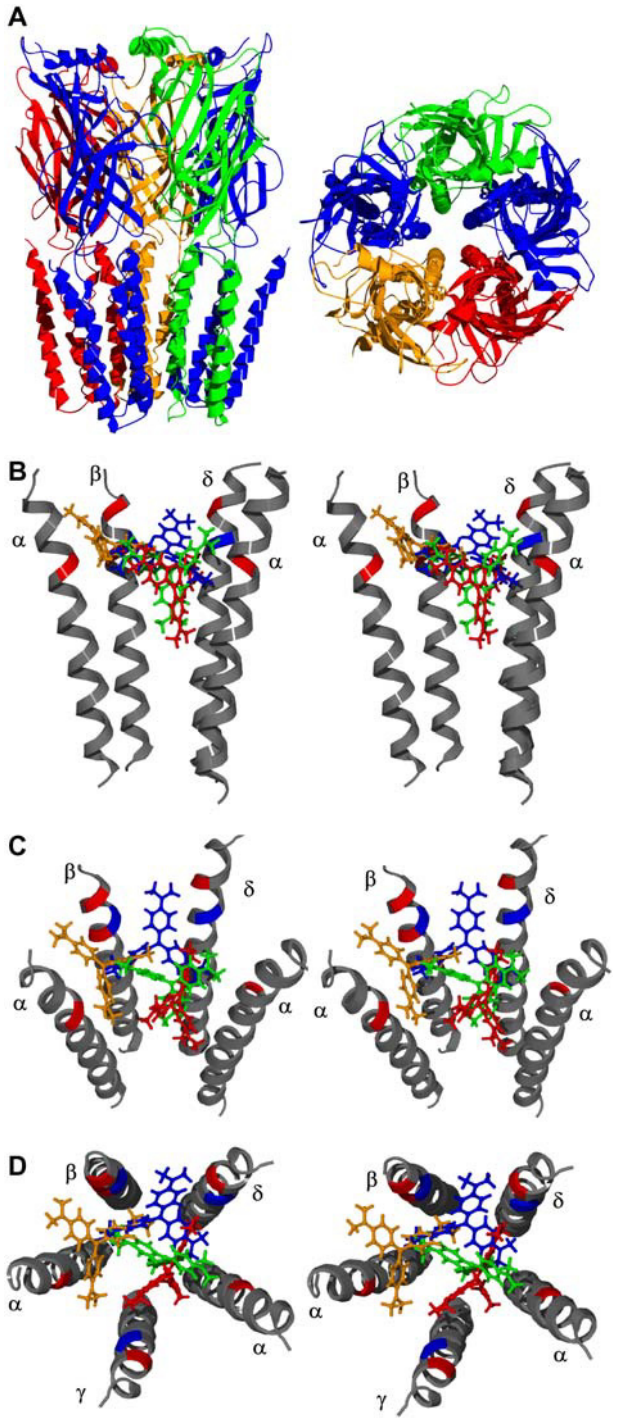

FIGURE 1 Homology model of the nAChR. (*A*) The pentamer comprises α(*blue*), β(*red*), γ(*green*), and δ(*orange*) *Torpedo californica* subunits, shown with vertical (*left*) or top down (*right*) orientations. (*B*) Stereo view of CrV within the nAChR lumen as positioned according to FRET measurements (*green*) and the three bound structures determined from Autodock simulations. Charged M2 residues are indicated in red (acidic) and blue (basic) on the ribbon-backbone trace. (*C*) Angled representation of the structures shown in *B*. (*D*) Top-down view of the same structures shown in *B*.

To initially constrain the possible CrV binding loci within the pore, we determined the distance from DC6C bound to the agonist sites to CrV by FRET. DC6C and CrV have broad spectral overlap from 450 to 630 nm (Fig. 2 *A*). The Förster distance for energy transfer, R_0, was calculated from these spectral properties using Eq. 2. Assuming an average orientation factor of $\kappa^2 = 2/3$ yields $R_0 = 47$ Å (Table 1). To

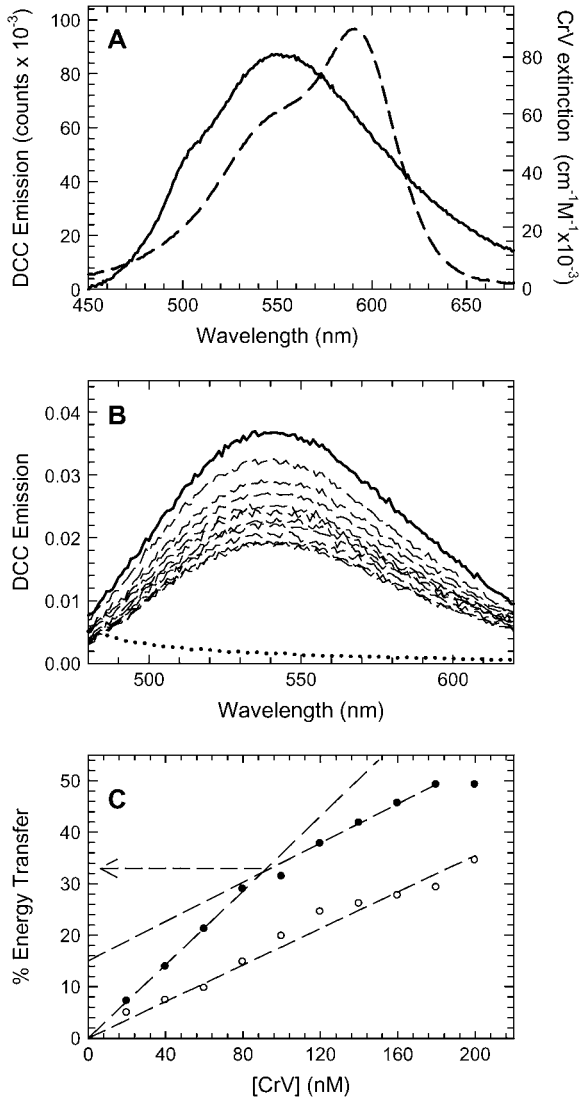

FIGURE 2 The distance from the agonist binding site to CrV measured by FRET. (*A*) Spectral overlap of DC6C fluorescent emission (*solid line*) and CrV absorbance (*dashed line*; data from Lurtz and Pedersen (16)) when bound to excess nAChR. (*B*) FRET measured by quenching of DC6C emission in the presence of CrV. The emission spectra of 200 nM DC6C in the presence of nAChR (100 nM) in the absence (*solid line*) or presence of 20–200 nM CrV (*dashed line*), and background fluorescence in the absence of DC6C (*dotted line*) are shown. (*C*) FRET efficiency plotted versus CrV concentration with (○) and without (●) 25 μM phencyclidine. The dashed lines are asymptotes drawn to the initial and final changes in FRET as described in the Materials and Methods. The arrow indicates the FRET efficiency at stoichiometrically bound DC6C and CrV.

constrain the uncertainty in R_0 due to κ^2, which can vary between 0 and 4, upper and lower limits of κ^2 were estimated from the fluorescence anisotropy of bound DC6C and bound CrV using the analysis of Dale et al. (18) (Eqs. 4–6). Remarkably, CrV anisotropy was small at excitation wavelengths near 550 nm and increased at higher wavelengths near 590 nm. The low anisotropy at 550 nm may be due to internal conversion of the excited state to a lower energy level with threefold degeneracy that arises from the threefold molecular symmetry. At the peak absorbance of CrV at 590 nm, the lower and upper limits on κ^2 (Table 1) leads to a 10-Å uncertainty in the R_0 value; at 550 nm R_0 has a 5-Å uncertainty.

Titration of the nAChR with CrV in 20-nM increments quenched the fluorescence emission from DC6C (Fig. 2, *B* and *C*) due to FRET. CrV was predominantly bound at low concentrations because the nAChR concentration was higher than the 10 nM K_D for CrV binding. At higher CrV concentrations, nonspecific binding produces a linear increase in background energy transfer that was also observed when specific CrV binding was inhibited by phencyclidine (Fig. 2 *C*, open circles). Energy transfer at stoichiometric occupancy was extrapolated from the intersection of the asymptotic lines to the initial rise and to the linear rise at high CrV concentrations. The efficiency of E = 33% ± 2.3% corresponds to a distance of R = 53 ± 0.9 Å with an uncertainty from κ^2 of 5–10 Å (Table 1).

DC6C was modeled into the agonist-binding sites of the nAChR as described in Materials and Methods. The 53-Å distance from the DC6C fluorophore to the central axis of the nAChR then placed CrV within the channel lumen near the extracellular mouth of the transmembrane region at the M2 α-helix outer ring of charged amino acids (Fig. 1). The uncertainty in distance gave an uncertainty along the central axis of the channel of ±4 Å. CrV was modeled into the structure and then energy minimized using Hyperchem (Fig. 1, *B–D*, *green*). On energy minimization, CrV shifted down the axis of the channel into a position 56 Å from the DC6C chromophore.

Autodock simulation of CrV binding (see Materials and Methods) yielded three distinct binding-mode populations, each with an internal RMSD less than 1 Å. All three were within the outer ring of charged residues as shown in Fig. 1, *B–D*. Model *a* (Fig. 1, *blue*) occurred in 55 of 100 simulations, model *b* (orange) in 16, and model *c* (red) in 29. The three modes bind CrV at distances of 51.9, 56.0, and 58.0 Å from the fluorophore of bound DC6C; these distances are consistent with the FRET measurements. The Autodock binding sites were eccentric and localized primarily at clefts between subunits, specifically at the $\delta\beta$, $\beta\alpha$, and $\alpha\gamma$ interfaces. Each binding mode had interactions with several negatively charged amino acids and was oriented to maximize electrostatic contacts.

TABLE 1 Spectral parameters of FRET between DC6C and CrV

J*	4.93×10^{-13} ($M^{-1}cm^3$)	
Q_0 (DC6C)	0.14	
η	1.4	
E	32.6% ± 2.3%†	
r_0 (DC6C)	0.28	
λ_{ex} for CrV	550 nm	590 nm
r_0 (CrV)	0.001	0.2
κ^2_{min}	0.37	0.19
κ^2_{max}	1.34	2.63
$R_{0\ min}$ (Å)	42	38
$R_{0\ avg}$ (Å)	47	48
$R_{0\ max}$ (Å)	52	58
R_{min} (Å)	47.4 ± 0.8	42.9 ± 0.8
R_{avg} (Å)	53.0 ± 0.9	54.2 ± 1.0
R_{max} (Å)	58.7 ± 1.0	65.5 ± 1.1

*The values for J, E, r_0, and κ^2 were determined as described in Materials and Methods. R_0 was calculated from Eqs. 2 and 1.
†Mean ± SE, n = 5.

Computation of AChR surface potentials

To account for partial ionization and shifted pK_a values on surface potentials, the ionization states of all titratable residues in the structure of the nAChR model were determined using UHBD, both with and without CrV bound (see Materials and Methods). The apparent pK_a values of the outer ring of charges are shown in Table 2 for low and high ionic strength conditions, without CrV bound. The environment in the pore significantly increased the pK_a values of the acidic residues, especially in low ionic strength, though less so for residues that appear to form salt bridges: residues δArg277 with αGlu262 and γLys272 with the second αGlu262. The sum of the partial charges in the outer ring is plotted versus pH at 20 mM and 300 mM ionic strength in Fig. 3. The net charge increases toward acidic pH, but less so in low ionic strength. Near physiological pH, the net charge immediately surrounding the CrV binding site is −3 in either ionic strength and essentially reflects the sum of charged residues.

TABLE 2 Ionization states of nAChR pore residues

	Apparent pK_a* for ionic strength		
Residue	20 mM	300 mM	Intrinsic pK_a†
α1Glu-262§	<2	4.66	4.25
α2Glu-262§	5.55	4.73	4.25
βAsp-268	6.22	5.50	3.65
βLys-269	>14	>14	10.53
βGlu-272	6.11	5.34	4.25
γLys-272§	>14	>14	10.53
γGlu-275	6.05	4.73	4.25
δArg-277§	>14	>14	12.48
δGlu-280	5.72	5.08	4.25

*Apparent pK_a values were computed using UHBD as described in Materials and Methods and are shown for two ionic strength conditions.
†The pK_a values of solitary amino acids in solution (47).
§Amino acid involved in salt-bridge contact.

To determine whether the computed pH dependence of the local charge environment was reflected in experimental determinations of pore properties, we examined the relationship of [^{3}H]phencyclidine binding energy to local charge. We used the pH dependence of binding from pH 4 to 9.5, shown in the accompanying article (10) and found a linear relationship between binding energies and the computed charge on outer ring at each pH (Fig. 3, *inset*). Comparison of the binding energy at −3 pore charge with the binding energy extrapolated to neutrality suggests that ionic interactions contribute as much as −7.7 kcal/mol of binding energy.

Fig. 4 *A* shows the computed potential juxtaposed with the structure of the nAChR. The electrostatic potential along the axis of the ion conductive channel was extracted from these results at various ionic strengths (Fig. 4 *B*, *red lines*). The vestibule and pore of nAChR have three peaks of electronegative potential that correspond to the extracellular mouth of the vestibule, the midpoint of the extracellular vestibule, and the extracellular ring of charge. The middle peak corresponded to a random coil section of the protein structure between the fifth and sixth β-strands. Lower ionic strength enhanced the potential by reduced electrostatic screening. Within the transmembrane region, the potential was positive crossing the membrane and became somewhat electronegative again at the intracellular mouth of the transmembrane region. However, potentials in this region do not include possible influence by the intracellular domains of the nAChR. For comparison, we plotted the potential derived from the transmembrane domain alone (blue line), which shows that the peak potential is enhanced somewhat by the presence of the vestibule. The presence of CrV shows that its influence on the potential (at 300 mM ionic strength, green line) is small and localized to the immediate area at the outer ring of charges.

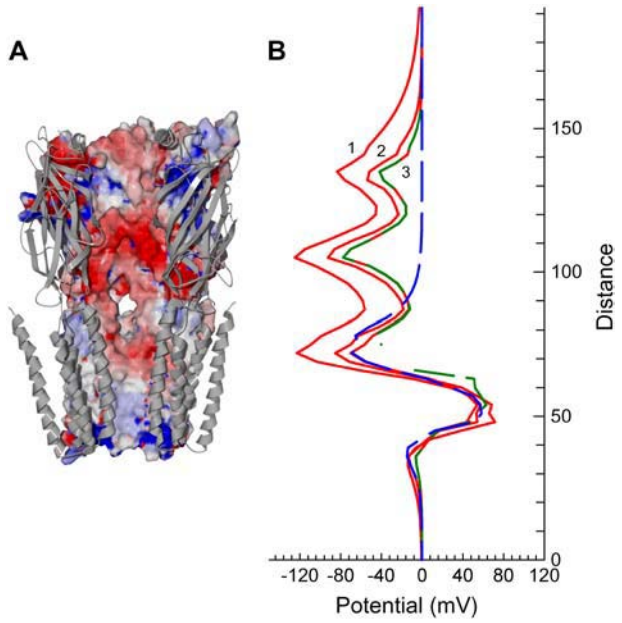

FIGURE 4 Vestibular and pore potentials of the nAChR. (*A*) Electrostatic potentials computed in 150 mM ionic strength are rendered with red as negative potential and blue as positive potential. The γ-subunit is removed, and α-subunits are rendered as ribbon structure to visualize the surface of the pore lumen. (*B*) Electrostatic potentials along the ion conductive pore axis were extracted from Poisson-Boltzmann computations solved on a grid with 3-Å spacing. Potential traces are plotted for nAChR (1, 20 mM; 2, 150 mM; 3, 300 mM ionic strength, *red*), the nAChR transmembrane domain (*blue*), and the nAChR with bound CrV in 300 mM ionic strength (*green*).

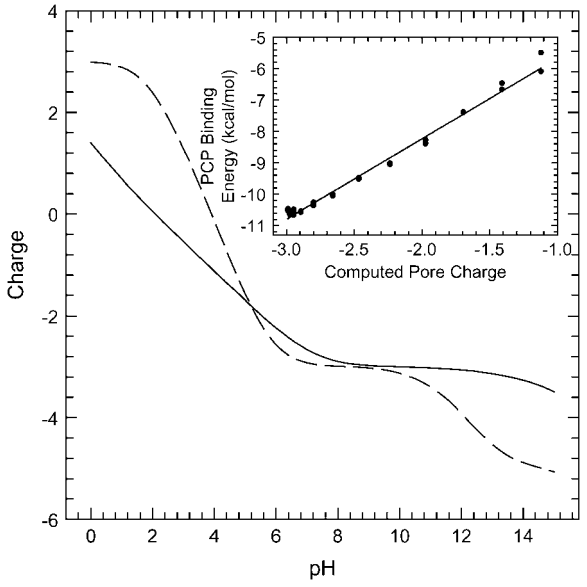

FIGURE 3 Simulated titration curves for charged amino acids at the CrV binding site. Titration curves were computed for 20 mM ionic strength (*solid line*) and 300 mM ionic strength (*dashed line*) as described in the text. (*Inset*) The effect of pH on [^{3}H]phencyclidine affinity in low ionic strength. Phencyclidine binding constants from Fig. 7 *B* of Meltzer et al. (10) at various pH values were converted to free energies in kcal/mol using the equation $\Delta G^0 = RT \ln K_D$. These binding energies are plotted against the computed charge at the pH for each datum. The fit line gives an intercept of −3.11 kcal/mol at zero charge and a slope of 2.56 kcal/mol/charge.

To determine the effects of local potentials on ionic currents through the channel, we calculated the relative flux of sodium and chloride ions for a range of transmembrane potentials using an equation derived from the Poisson-Nernst-Plank equation (32). This calculation considers only the influence of electrostatic forces from the axial potentials; the effects of ion concentration, close interactions with the protein surface, and binding events are not addressed. For the homology model, the inward flux of Na^+ ions displays some inward rectification (Fig. 5, *solid circles*). To understand the nonlinearity in the current-voltage relationship, we also analyzed the transmembrane domain alone (without the vestibular region, *solid squares*). The transmembrane domain displays a nearly linear relationship, suggesting that vestibular charges impart rectification. We also examined anion flux for both structures (Fig. 5, *open symbols*). At

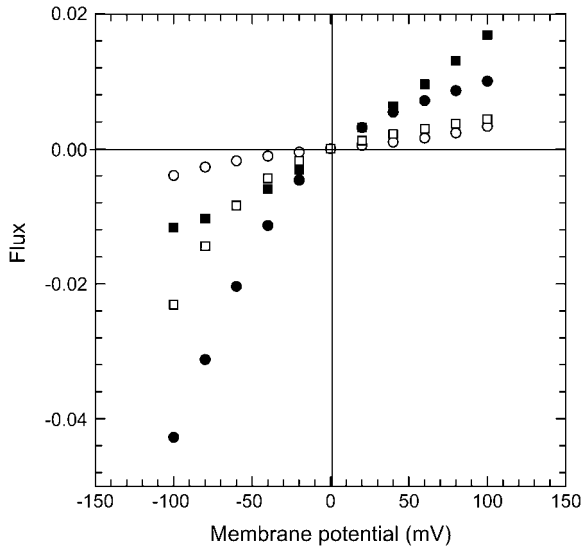

FIGURE 5 Inward rectification is caused by the nAChR vestibular potential. The relative ion flux for Na^+ (●, ■) and Cl^- (○, □) is plotted versus the membrane potential. Flux is compared for the homology model of the nAChR (○, ●) and for the transmembrane domain alone (□, ■). Relative flux was calculated using Eq. 9 as described in Methods.

negative potentials, chloride flux is about 10-fold lower than sodium flux. For the transmembrane domain alone, chloride flux is comparable to sodium flux at negative potentials, whereas it is smaller at positive potentials and displays some rectification.

Simulation of DEFET-determined rate constants and potentials

To test the consistency of the computed versus experimental local surface electrostatic potentials, we compared actual DEFET values (10) with computed DEFET rates of the Tb^{3+} chelates (k_2^x). The rates were calculated from the structural models of the CrV-bound nAChR and the corresponding UHBD-computed potentials by numerical integration of Eq. 7. Because k_2^x values depend on the donor-acceptor distances (r) as r^{-6}, the largest contributions to k_2^x arise from the closest approach of the donor–acceptor pair and renders computation of k_2^x sensitive to the details of the acceptor environment. Therefore, we examined the response of the computation to several parameters, including the size and spacing of the grid that described the chelate-accessible space, the presumed radius of the Tb^{3+} chelate, the position of the dipole within the CrV structure, and the various models of CrV binding within the pore. Computed k_2^0 values were relatively constant when grid spacing was varied in the range of 0.4–1 Å; below this range, k_2^0 dropped because insufficient volume was sampled (data not shown).

To obtain the radius of the Tb^{3+} chelates for the computation, we examined the structure of a closely related chelate, Er-EDTA-trihydrate (33). Tb^{3+} has an ionic radius nearly identical to Er^{3+}, and Tb-EDTA (Tb^-) is likewise triply hydrated (34). Erbium is located eccentrically within the roughly spherical chelate with distances from the Er-atom center to the periphery between 4 and 6 Å. We expect that rapid rotation of freely diffusing chelates during the ~1 ms lifetimes should yield an averaged, effective radius biased by the r^{-6} dependence of energy transfer. The FRET distance, r, the distance between the emission and absorption dipoles, also depends on the position of the CrV absorption dipoles. Because the CrV dipoles are not known precisely (35) and have threefold degeneracy, we calculated this distance in two ways: from the Tb^{3+} center to the nearest CrV atom center (method 1) or to the center atom of CrV (method 2).

Because the presumed chelate radius determines the FRET distance and affects the integrated volume, k_2^0 values to free and bound CrV were computed using various chelate radii (Fig. 6 *A*). The FRET distances were computed using both dipole methods for the neutral chelate, Tb^0, to avoid electrostatic effects. For free CrV, k_2^0 values for the two distance methods bracket the observed value at all radii, whereas for bound CrV, both methods underestimated the observed value, except at the smaller radii with method 1. The k_2^0 values were strongly dependent on chelate radius, varying ~10-fold for free CrV and as much as 100-fold for bound CrV. On this basis, a single, effective radius that described k_2^0 values could not be chosen. However, when we examined the influence of electrostatic potentials on DEFET by computing potentials from the ratios of k_2^x values for variously charged chelates using Eq. 8 (Fig. 6 *B*), there was more consistency. For such potentials, there was virtually no difference between methods 1 and 2, and the dependence on chelate radius was smaller. Furthermore, there is good agreement for the potential near free CrV at the smaller radii. The better agreement for potentials, as compared with raw k_2^x values, is expected from examination of Eq. 7. The spectral properties of the chelates are similar, and their lifetimes were determined with high precision; therefore, it can be shown that the ratio of k_2^x for two chelates will depend exclusively on the sampled volume and the corresponding electrostatic potential (36). Thus, the approximation to the local potential from the Boltzmann distribution (Eq. 8) represents a better point of comparison than raw k_2^x values.

The position of CrV within the pore of the receptor also influenced the predicted k_2^x values. Fig. 6 *C* illustrates the differences between the experimentally determined k_2^x values and the values obtained for the three Autodock structures and the structure with CrV positioned according to the FRET distance measurement, as computed with a 5-Å chelate radius and distance method 1. The Autodocked structures have smaller k_2^x values that reflect a smaller exposed ligand surface area than the FRET-positioned molecule. Nonetheless, when the local potentials are computed, they are all similar (Fig. 6 *D*). In each case, the predicted local potential

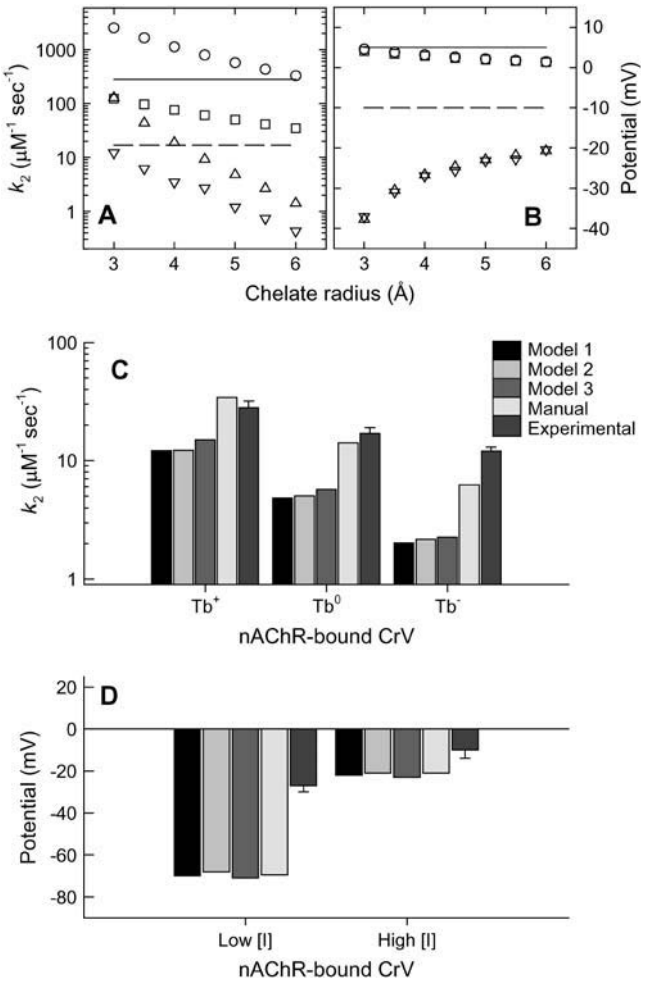

FIGURE 6 Computational simulation of DEFET from Tb^{3+} chelates to CrV. (*A*) Energy transfer rate constants (k_2^0) were computed for Tb^0 DEFET to CrV free in solution (○, □) or bound to the nAChR (△,▽) with varying radii for the chelate. CrV binding was modeled according to Autodock model 1. Energy transfer was computed using the distance from Tb^0 to nearest CrV atom (method 1, ○, △) or to its central atom (method 2, □,▽). The experimentally determined k_2^0 values for free (*solid line*) and bound CrV (*dashed line*) are shown for comparison (10). (*B*) Local potentials as a function of chelate radius. Energy transfer rates for Tb^0, Tb^-, and Tb^+ were computed to free (○, □) and bound CrV (△, ▽) and included the effects of the UHBD-derived local surface electrostatic potential, assuming an ionic strength of 300 mM. The local potentials near CrV were computed using the Boltzmann distribution from the ratios of k_2^x using Eq. 8, at various chelate radii. For comparison, the experimentally determined values are shown for free (*solid line*) and nAChR-bound CrV (*dashed line*). Computations were carried out with both the distances to CrV atom by method 1 (○, △) and method 2 (□, ▽). (*C*) Comparison of energy transfer rates for the free and various bound CrV structures. Models 1–3 are the Autodocked structures; *Manual* refers to the bound CrV model derived from FRET distance-based positioning. All computations were solved at 300 mM ionic strength at pH 7.0 with a 5-Å chelate radius. (*D*) Local potentials were computed using Eq. 8 for free and bound CrV at two ionic strengths: 20 mM (*Low*) and 300 mM (*High*).

is nearly twofold stronger than that measured experimentally. In contrast, for free CrV, the computed k_2^x values overestimate the experimental values (method 1, Fig. 6 *A*) and underestimate the experimental potential (Fig. 6 *B*).

DISCUSSION

The nAChR has a large extracellular anionic vestibule and an annular ring of charges near the pore entrance, the outer ring (1), whose electrostatic surface potentials have been proposed to influence conduction and ionic selectivity. In the accompanying article (10), DEFET measurements of potential near the outer ring showed only modest potentials on the order of −10 mV at physiological ionic strength. In this article, we computed surface potentials and from them calculated expected DEFET rates to Tb^{3+} chelates for direct comparison with DEFET experiments. The computed pore potentials show that the large anionic vestibule contributes a small component to the potentials at the pore entrance. Potentials from calculated DEFET rate ratios using the Boltzmann approximation consistently overestimated the experimentally determined potentials, suggesting a systematic error in either the experiment or computation.

The outer ring charges

The outer ring of charges in the M2 transmembrane helix of the AChR affects conduction to a smaller extent than those in the intermediate ring and in the inner ring of charges, as originally demonstrated by Imoto et al. (1) using site-directed mutagenesis and measurements of single-channel conductance. Assuming that the observed conductance changes reflect changes in local surface potential, their conductance change from ~80 pS to ~60 pS on a charge change from −3 to zero corresponds to a potential of about −7 mV, a value consistent with our DEFET measurements (10). Kienker et al. (37) further investigated the role of outer ring charges by site-directed mutagenesis and measuring conductance changes in varying ionic strengths. The changes in conductance were independent of ionic strength, an observation that is inconsistent with purely electrostatic effects on conductance. To model their results, they suggested that these residues include a component of ion binding. The substituted cysteine accessibility approach measured a potential gradient in the pore that decreased in magnitude near the extracellular side of M2, consistent with a weak potential at the outer ring (7).

Ligand-binding measurements in varying ionic strength also provided indirect measures of surface potential in this region. Herz et al. (38) found that ions inhibit ethidium binding, and Song and Pedersen (12) found such ionic strength effects to be consistent with electrostatic screening; in neither case were the data interpreted directly in terms of electrostatic surface potentials. Ionic strength dependence of [^{3}H]phencyclidine binding analyzed by a modified Debye-Hückel equation indicated the presence of −3.3 charges, which is in remarkably good agreement with the computed net −3 charge of the outer ring (10). In contrast, pH titration caused large changes in [^{3}H]phencyclidine affinity, suggesting a strong dependence on charge interactions. If we assume that pH effects were mediated by long-range electrostatic

interactions, then the titration data correspond to a negative potential of about −300 mV (from $\Delta V = \Delta G^0/zF$; ΔG^0 is taken from the slope of Fig. 3, *inset*). The stark discrepancy with other estimates suggests that the interactions that drive noncompetitive antagonist binding may include close interactions and dehydration, which may be affected by pH but not by ionic strength.

Except for the pH titration data, these experimental determinations of potential at the outer ring of charges are reasonably consistent with the −10 mV value determined by DEFET (10), which is too small to be the primary determinant of selectivity and conductance. Notably, the DEFET measurement is of the net potential at the CrV site and includes contributions from the vestibule as well as localized contributions from the outer ring charges. We conclude that the contribution of vestibular charge to electrostatic attraction at the pore entrance is small.

Computed surface potentials

Theoretical work has predicted that a modest number of charges near a pore restriction may profoundly affect ionic conduction and selectivity (4,39) and that overall charge density in the vestibule can influence the magnitude of the potential at the pore restriction and thereby contribute to conduction and selectivity (3). One caveat is that locally high charge densities may undergo a significant degree of self-neutralization. Self-consistent computation of pK values using the Bashford and Karplus approach (31) in the UHBD program in the vicinity of the outer ring shows that in the physiological pH range there is little self-neutralization (Fig. 3). The stability of net charge in the physiological range may come from the close apposition of several cationic lysines and arginines near the anionic residues.

The computed surface potentials revealed sizable negative potentials near the mouth of the pore at the apex of the M2-α-helices and near the middle of the extracellular vestibule (Fig. 4) sufficient to exert an influence on conduction and selectivity. Comparison of the calculated conductivity of Na^+ versus Cl^- (Fig. 5) shows that these potentials could account for as much as a 10-fold selectivity, with the primary contribution from the charges in the vestibule; the outer ring charges, per se, provide little selectivity. The nAChR selectivity of Na^+ over Cl^- is more than 100-fold (40); therefore, the most likely region of the nAChR to primarily determine cation selectivity appears to be the intracellular mouth of the transmembrane region (1,41) rather than the vestibule. The conductivity calculations also indicate rectification, arising from the vestibular charges, that is stronger than observed in symmetrical salt for the mouse muscle nAChR (37,42). The model used for these computations lacked the intracellular domain structure and its associated charge. Extending the lumen of the channel by 30 Å and modeling an additional intracellular region of negative charge reduced the inward rectification (data not shown). This observation suggests that the electronegative charge observed in the extracellular vestibule may be functionally balanced by a similar charge distribution in the intracellular domain.

Comparison of computed and experimentally determined potentials

One concern for the DEFET experiments was that the added charge of CrV and its binding interactions with nearby acidic residues would obscure features of the potential that might be present in its absence. However, as seen in Fig. 4, the computed potential was lessened only slightly by CrV at the outer ring of charges. Direct comparison of experimental to computed DEFET rate constants (k_2^x) proved difficult because of the sensitivity of the computed k_2^x values to the assumed chelate size and the uncertainty of the dipole location within the acceptor. Estimates of the potential using the Boltzmann distribution, however, yielded values that were insensitive to the choice of acceptor dipole, and the effects of chelate size were ameliorated. This estimate of the potential is more robust because it relies on the ratio of k_2^x values, and most factors that influence energy transfer cancel within the ratio [for a detailed derivation see Meltzer (36)]. These values, which vary from −40 to −20 mV depending on chelate size, are smaller than the −70 mV axial potential near the vestibule. Thus, according to the computation, the potential estimated with the Boltzmann distribution from the DEFET approach may underestimate the underlying potential by a factor of two to three. This is not surprising because the DEFET measurements are integrated over a volume of space that varies in potential.

The potentials derived from computed DEFET rates, nevertheless, overestimate the potentials based on experimental DEFET results by two- to fourfold. The source of this discrepancy may arise from either experimental or computational error. Experimentally, an underestimate of the potential could result from underestimated DEFET constants for the positive chelate and overestimated constants of the negative chelate. Such a situation could arise from the presence of unbound CrV in the samples; however, we measured free CrV to be $<1\%$ of the CrV added, and correction for this amount did not change the results substantially. Although the rate of energy transfer from the negative chelate was near the lower limit of detection, higher DEFET rates to the positive chelate potential should have been readily observed. Therefore, we do not believe that simple error in the DEFET measurements accounts for the difference in estimates.

Systematic errors in the computed potentials could arise from an incorrect protein structure, a mistaken CrV binding locus, the UHBD-derived estimates of potential, or the numerical integration of DEFET rates. The homology structure used in the computations also does not include bound Ca^{2+} ions, glycosyl groups, or tightly bound lipid. Each of these might influence the electrostatic potential computed near the

site of bound CrV. The nAChR transmembrane domain model is likely representative of the nAChR resting conformation rather than the desensitized state, which was stabilized during the experiment. A distinct arrangement of ionic residues in the desensitized state could conceivably yield a distinct, smaller potential in the vicinity of the CrV binding site. We tested four orientations of CrV from Autodock- or FRET-based placement that all yielded similar potentials (Fig. 6). Each model was consistent with the FRET-based distance measurement and with the labeling site of meproadifen mustard (43); other noncompetitive antagonists such as chlorpromazine (44) and TID (45), however, appear to reside more deeply in the pore. One gauge of whether the binding model is realistic is to examine the relative accessibility of CrV by the ratio of the DEFET rates for receptor-bound and free CrV from the neutral chelate, k_2^0, (Fig. 6 *A*). This value is smaller for the computed values and suggests that the binding model represents a more restricted space than observed experimentally.

Direct comparison of computed and experimental DEFET rates assumes that all energy transfer occurs by dipolar mechanisms. Dipolar energy transfer calculations may underestimate the true rate of donor quenching if additional mechanisms, such as collisional quenching or electron exchange (46), occur. In the case of collisional quenching, there could be some effect on the estimated potential as well, although it should still reflect local changes in donor concentration due to electrostatic interactions, but the spatial integration will be confined to the region of contact with CrV.

Poisson-Boltzmann computation of electrostatic potentials may misrepresent potentials in regions where the dimensions of the solvent space approach the Debye length for ionic screening, such as occurs in the ion channel vestibules because ions will not occupy this space at all times. As articulated by Moy et al. (11), Poisson-Boltzmann calculations in such regions may account for too much ionic screening and, therefore, underestimate the local potential at physiological ionic strengths. It was argued that Brownian dynamics simulations may provide better estimates. In contrast, we computed Poisson-Boltzmann potentials that overestimated the experimental potentials. In addition, we observed substantial effects of ionic strength on the potential in both experiments and computations (Fig. 6 *C*). It is possible, therefore, that the Poisson-Boltzmann approximations are valid when time-averaged, though perhaps not at any one instant where the ionic composition may deviate from the average.

SUMMARY AND CONCLUSIONS

Few approaches to experimentally determining electrostatic surface potentials are completely satisfactory because compounds that vary in charge often also vary in hydration, hydrophobicity, solubility, or reactivity. The Tb^{3+} chelate approach for determining potentials directly compares charged chelates that are similar in structure and chemical properties and thus overcomes most of these problems. A second advantage of this approach is that the DEFET measurements have a sound theoretical basis that permits direct comparison of computed and measured potentials. Such comparisons provide a critical evaluation of each approach that is needed for future determinations of the effects of electrostatics on protein function. In this case, we have experimental results that are smaller than computed potentials by a factor of two to four. This degree of agreement provides confidence that the data provide realistic estimates of pore potentials. Nonetheless, it will be of interest to examine the basis for the discrepancies more closely.

The authors thank Manali Joshi for fruitful scientific discussions regarding the computational work.

This work was supported by grant NS 35212 (S.E.P.) from the U.S. Public Health Service, grant E-1497 (J.M.B.) from the Robert A. Welch Foundation, and funding from National Aeronautics Space Administration through the University Research Center at Texas Southern University (J.M.B.). R.H.M. was supported by grants T32 HL07676 to the Department of Molecular Physiology and Biophysics and T32-GM088280 to the Houston Area Molecular Biophysics Program. W.V.C. was supported by National Science Foundation predoctoral fellowship DGE-9255674.

REFERENCES

1. Imoto, K., C. Busch, B. Sakmann, M. Mishina, T. Konno, J. Nakai, H. Bujo, Y. Mori, K. Fukuda, and S. Numa. 1988. Rings of negatively charged amino acids determine the acetylcholine receptor channel conductance. *Nature*. 335:645–648.
2. Sansom, M. S., C. Adcock, and G. R. Smith. 1998. Modelling and simulation of ion channels: applications to the nicotinic acetylcholine receptor. *J. Struct. Biol*. 121:246–262.
3. Adcock, C., G. R. Smith, and M. S. Sansom. 1998. Electrostatics and the ion selectivity of ligand-gated channels. *Biophys. J*. 75:1211–1222.
4. Dani, J. A. 1986. Ion-channel entrances influence permeation. Net charge, size, shape, and binding considerations. *Biophys. J*. 49:607–618.
5. Adcock, C., G. R. Smith, and M. S. Sansom. 1998. Electrostatics of ligand-gated ion channels. *Biochem. Soc. Trans*. 26:S300.
6. Northrup, S. H., T. G. Wensel, C. F. Meares, J. J. Wendoloski, and J. B. Matthew. 1990. Electrostatic field around cytochrome c: theory and energy transfer experiment. *Proc. Natl. Acad. Sci. USA*. 87:9503–9507.
7. Pascual, J. M., and A. Karlin. 1998. State-dependent accessibility and electrostatic potential in the channel of the acetylcholine receptor. Inferences from rates of reaction of thiosulfonates with substituted cysteines in the M2 segment of the alpha subunit. *J. Gen. Physiol*. 111:717–739.
8. Wensel, T. G., C. H. Chang, and C. F. Meares. 1985. Diffusion-enhanced lanthanide energy-transfer study of DNA-bound cobalt(III) bleomycins: comparisons of accessibility and electrostatic potential with DNA complexes of ethidium and acridine orange. *Biochemistry*. 24:3060–3069.
9. Wensel, T. G., and C. F. Meares. 1983. Electrostatic properties of myoglobin probed by diffusion-enhanced energy transfer. *Biochemistry*. 22:6247–6254.
10. Meltzer, R. H., M. M. Lurtz, T. G. Wensel, and S. E. Pedersen. 2006. Nicotinic acetylcholine receptor channel electrostatics determined by diffusion-enhanced luminescence energy transfer. *Biophys. J*. 91:1315–1324.
11. Moy, G., B. Corry, S. Kuyucak, and S. H. Chung. 2000. Tests of continuum theories as models of ion channels. I. Poisson-Boltzmann theory versus Brownian dynamics. *Biophys. J*. 78:2349–2363.

12. Song, X. Z., and S. E. Pedersen. 2000. Electrostatic interactions regulate desensitization of the nicotinic acetylcholine receptor. *Biophys. J.* 78:1324–1334.

13. Waksman, G., M. C. Fournie-Zaluski, and B. Roques. 1976. Synthesis of fluorescent acyl-cholines with agonistic properties: pharmacological activity on *Electrophorus* electroplaque and interaction in vitro with *Torpedo* receptor-rich membrane fragments. *FEBS Lett.* 67:335–342.

14. Herz, J. M., D. A. Johnson, and P. Taylor. 1989. Distance between the agonist and noncompetitive inhibitor sites on the nicotinic acetylcholine receptor. *J. Biol. Chem.* 264:12439–12448.

15. Lakowicz. 1983. Principles of Fluorescence Spectroscopy. Plenum Press, New York.

16. Lurtz, M. M., and S. E. Pedersen. 1999. Aminotriarylmethane dyes are high-affinity noncompetitive antagonists of the nicotinic acetylcholine receptor. *Mol. Pharmacol.* 55:159–167.

17. Johnson, D. A., J. G. Voet, and P. Taylor. 1984. Fluorescence energy transfer between cobra alpha-toxin molecules bound to the acetylcholine receptor. *J. Biol. Chem.* 259:5717–5725.

18. Dale, R. E., J. Eisinger, and W. E. Blumberg. 1979. The orientational freedom of molecular probes. The orientation factor in intramolecular energy transfer. *Biophys. J.* 26:161–193.

19. Noda, M., H. Takahashi, T. Tanabe, M. Toyosato, S. Kikyotani, Y. Furutani, T. Hirose, H. Takashima, S. Inayama, T. Miyata, and S. Numa. 1983. Structural homology of *Torpedo californica* acetylcholine receptor subunits. *Nature.* 302:528–532.

20. Noda, M., H. Takahashi, T. Tanabe, M. Toyosato, S. Kikyotani, T. Hirose, M. Asai, H. Takashima, S. Inayama, T. Miyata, and S. Numa. 1983. Primary structures of beta- and delta-subunit precursors of *Torpedo californica* acetylcholine receptor deduced from cDNA sequences. *Nature.* 301:251–255.

21. Noda, M., H. Takahashi, T. Tanabe, M. Toyosato, Y. Furutani, T. Hirose, M. Asai, S. Inayama, T. Miyata, and S. Numa. 1982. Primary structure of alpha-subunit precursor of *Torpedo californica* acetylcholine receptor deduced from cDNA sequence. *Nature.* 299:793–797.

22. Gotoh, O. 1999. Multiple sequence alignment: algorithms and applications. *Adv. Biophys.* 36:159–206.

23. Sine, S. M., H. L. Wang, and N. Bren. 2002. Lysine scanning mutagenesis delineates structural model of the nicotinic receptor ligand binding domain. *J. Biol. Chem.* 277:29210–29223.

24. Guex, N., and M. C. Peitsch. 1997. SWISS-MODEL and the Swiss-PdbViewer: an environment for comparative protein modeling. *Electrophoresis.* 18:2714–2723.

25. Brooks, B. R., R. E. Bruccoleri, B. D. Olafson, D. J. States, S. Swaminathan, and M. Karplus. 1983. CHARMM: a program for macromolecular energy, minimization, and dynamics calculations. *J. Comput. Chem.* 4:187–215.

26. Miyazawa, A., Y. Fujiyoshi, and N. Unwin. 2003. Structure and gating mechanism of the acetylcholine receptor pore. *Nature.* 423:949–955.

27. Brejc, K., W. J. van Dijk, R. V. Klaassen, M. Schuurmans, J. van Der Oost, A. B. Smit, and T. K. Sixma. 2001. Crystal structure of an ACh-binding protein reveals the ligand-binding domain of nicotinic receptors. *Nature.* 411:269–276.

28. Dewar, M. J. S., E. G. Zoebisch, E. F. Healy, and J. J. P. Stewart. 1985. AM1: a new general purpose quantum mechanical molecular model. *J. Am. Chem. Soc.* 107:3902–3909.

29. Morris, G. M., D. Goodsell, R. S. Halliday, R. Huey, W. E. Hart, R. K. Belew, and A. J. Olson. 1998. Automated docking using a Lamarckian genetic algorithm and an empirical binding free energy function. *J. Comput. Chem.* 19:1639–1662.

30. Madura, J. D., J. M. Briggs, R. C. Wade, M. E. Davis, B. A. Luty, A. Ilin, J. Antosiewicz, M. K. Gilson, B. Bagheri, L. R. Scott, and J. A. McCammon. 1995. Electrostatics and diffusion of molecules in solution - simulations with the University of Houston Brownian Dynamics Program. *Comp. Phys. Commun.* 91:57–95.

31. Bashford, D., and M. Karplus. 1990. pK_a's of ionizable groups in proteins: atomic detail from a continuum electrostatic model. *Biochemistry.* 29:10219–10225.

32. Adcock, C., G. R. Smith, and M. S. Sansom. 2000. The nicotinic acetylcholine receptor: from molecular model to single-channel conductance. *Eur. Biophys. J.* 29:29–37.

33. Sakagami, N., Y. Yamada, T. Konno, and K. Okamoto. 1999. Crystal structures and stereochemical properties of lanthanide (III) complexes with ethylenediamine-*N,N,N′,N′*-tetraacetate. *Inorg. Chim. Acta.* 288: 7–16.

34. Horrocks, W. D., Jr., and D. R. Sudnick. 1979. Lanthanide ion probes of structure in biology. laser-induced luminescence decay constants provide a direct measure of the number of metal-coordinated water molecules. *J. Am. Chem. Soc.* 101:334–340.

35. Lovell, S., B. J. Marquardt, and B. Kahr. 1999. Crystal violet's shoulder. *J. Chem. Soc., Perkin Trans. 2.*2241–2247.

36. Meltzer, R. H. 2004. Protein Electrostatics and the Function of the Nicotinic Acetylcholine Receptor. Baylor College of Medicine, Houston, TX.

37. Kienker, P., G. Tomaselli, M. Jurman, and G. Yellen. 1994. Conductance mutations of the nicotinic acetylcholine receptor do not act by a simple electrostatic mechanism. *Biophys. J.* 66:325–334.

38. Herz, J. M., S. J. Kolb, T. Erlinger, and E. Schmid. 1991. Channel permeant cations compete selectively with noncompetitive inhibitors of the nicotinic acetylcholine receptor. *J. Biol. Chem.* 266:16691–16698.

39. Jordan, P. C. 1987. How pore mouth charge distributions alter the permeability of transmembrane ionic channels. *Biophys. J.* 51:297–311.

40. Adams, D. J., T. M. Dwyer, and B. Hille. 1980. The permeability of endplate channels to monovalent and divalent metal cations. *J. Gen. Physiol.* 75:493–510.

41. Unwin, N. 2005. Refined structure of the nicotinic acetylcholine receptor at 4Å resolution. *J. Mol. Biol.* 346:967–989.

42. Dani, J. A. 1988. Ionic permeability and the open channel structure of the nicotinic acetylcholine receptor. *In* Transport through Membranes: Carriers, Channels and Pumps. A. Pullman, J. Jortner, and B. Pullman, editors. Kluwer Academic Publishers, Dordrecht, The Netherlands. 297–319.

43. Pedersen, S. E., S. D. Sharp, W. S. Liu, and J. B. Cohen. 1992. Structure of the noncompetitive antagonist-binding site of the *Torpedo* nicotinic acetylcholine receptor. *J. Biol. Chem.* 267:10489–10499.

44. Dennis, M., J. Giraudat, F. Kotzyba-Hibert, M. Goeldner, C. Hirth, J. Y. Chang, C. Lazure, M. Chretien, and J. P. Changeux. 1988. Amino acids of the *Torpedo marmorata* acetylcholine receptor alpha subunit labeled by a photoaffinity ligand for the acetylcholine binding site. *Biochemistry.* 27:2346–2357.

45. White, B. H., and J. B. Cohen. 1992. Agonist-induced changes in the structure of the acetylcholine receptor M2 regions revealed by photoincorporation of an uncharged nicotinic noncompetitive antagonist. *J. Biol. Chem.* 267:15770–15783.

46. Meares, C. F., S. M. Yeh, and L. Stryer. 1981. Exchange interaction contribution to energy transfer between ions in the rapid-diffusion limit. *J. Am. Chem. Soc.* 103:1607–1609.

47. Lehninger, A. L., D. L. Nelson, and M. M. Cox. 1997. Principles of Biochemistry. Worth Publishers, New York.